RSC Advances

ROYAL SOCIETY OF CHEMISTRY

www.rsc.org/advances

Investigating the thermoelectric properties of *p*-type half-Heusler $Hf_x(ZrTi)_{1-x}CoSb_{0.8}Sn_{0.2}$ by reducing Hf concentration for power generation

Ran He, Hee Seok Kim, Yucheng Lan, Dezhi Wang, Shuo Chen*, and Zhifeng Ren*

Department of Physics and TcSUH, University of Houston, Houston, Texas 77204

Abstract

Based on the fact that Hf is much more expensive than other commonly used elements in HfCoSb-based half-Heusler materials, we studied the thermoelectric properties of the *p*-type half-Heusler $Hf_x(ZrTi)_{1-x}CoSb_{0.8}Sn_{0.2}$ by reducing Hf concentration. A peak *ZT* of ~1.0 was achieved at 700 °C with the composition of $Hf_{0.19}Zr_{0.76}Ti_{0.05}CoSb_{0.8}Sn_{0.2}$ by keeping the Hf/Zr ratio at 1/4 and Hf/Ti at 4/1. This composition has much reduced cost and similar thermoelectric performance compared with our previously reported best *p*-type half-Heusler: $Hf_{0.44}Zr_{0.44}Ti_{0.12}CoSb_{0.8}Sn_{0.2}$. Due to the decreased usage of Hf, it is more favorable for consideration in applications. In addition, a higher output power is expected because of the higher power factor even though the conversion efficiency is the same due to the same *ZT*.

Key words: Thermoelectric, Half-Heusler, Hf reduction, output power.

*To whom correspondence should be addressed.

1. Introduction

With the recent advance of high performance thermoelectric materials, such as half-Heusler,[1,2] PbTe,[3-5] Bi_2Te_3,[6] skutterudites,[7,8] SiGe,[9,10] $Mg_2Si_{1-x}Sn_x$,[11] $Ba_8Ga_{16}Ge_{30}$,[12] etc., thermoelectric generators based on these materials become promising in providing the needed clean energy to the modern society. The core parameter of a thermoelectric material is named the dimensionless figure of merit (ZT), $ZT = \frac{S^2}{\kappa\rho}T$, where S, ρ, κ, and T are the Seebeck coefficient, electrical resistivity, thermal conductivity, and absolute temperature, respectively. Among the various thermoelectric materials, half-Heusler (HH), especially MNiSn-based *n*-type and MCoSb-based *p*-type (M = Hf, Zr, Ti)[13-15] are of particular interests. A ZT as high as 1.5 was reported by S. Sakurada and N. Shutoh[16] in the MNiSn-based *n*-type HH. Unfortunately, this result was never repeated. But still, of HH, the thermal stability, non-toxicity, mechanical rigidity[17] combining with the decent ZT of ~1 makes them good candidates for moderate temperature (400-700 °C) applications such as waste heat recovery from vehicles and industrial plants.

For practical applications, low materials cost is desired. For example, skutterudites, specifically $Ba_{0.08}La_{0.05}Yb_{0.04}Co_4Sb_{12}$ at \$64/kg and $Ce_{0.45}Nd_{0.45}Fe_{3.5}Co_{0.5}Sb_{12}$ at \$103/kg based on the raw element cost are considered as acceptable.[18] Recently, we have realized a ~50 % cost reduction in the n-type HH (from \$234/kg of $Hf_{0.75}Zr_{0.25}NiSn_{0.99}Sn_{0.01}$ to \$113/kg of $Hf_{0.25}Zr_{0.75}NiSn_{0.99}Sn_{0.01}$).[2,19] In comparison, p-type $Hf_{0.44}Zr_{0.44}Ti_{0.12}CoSb_{0.8}Sn_{0.2}$ at \$174/kg is still too expensive. Such a high cost originates from the overwhelmingly expensive Hf. From Table 1, a simple calculation indicates that about 85% of the total material cost comes from Hf in $Hf_{0.44}Zr_{0.44}Ti_{0.12}CoSb_{0.8}Sn_{0.2}$. Therefore, reducing the usage of Hf is the key to achieve low cost HH for practical applications.

Table 1. Price of the commonly used elements in half-Heusler materials using the price of elements in year 2010.[20]

Elements	Hf	Zr	Ti	Co	Ni	Sb	Sn

Price ($/kg)	563	99.76	10.74	45.97	21.8	8.84	27.34

The investigation on reducing Hf usage in MCoSb HH is based on our previously optimized composition by Yan *et al.*,[21] $Hf_{0.8}Ti_{0.2}CoSb_{0.8}Sn_{0.2}$ with ZT ~1 at 800 °C, where the ratio of Hf to Ti is 4/1. Keeping a similar Hf/Ti ratio (atomic ratio and hereafter), ~4/1, $Hf_{0.44}Zr_{0.44}Ti_{0.12}CoSb_{0.8}Sn_{0.2}$ was found to have a similar ZT ~1.0 at 700 °C. Realizing that the Hf concentration is still too high, we investigated the reduction of Hf by Zr in this work and found the best composition is $Hf_{0.19}Zr_{0.76}Ti_{0.05}CoSb_{0.8}Sn_{0.2}$. By doing so, we have succeeded in reducing the usage of Hf to below 0.2 in the MCoSb system while keeping a similar ZT of ~1.0 at 700 °C. This composition results in a ~40% cost reduction comparing with $Hf_{0.44}Zr_{0.44}Ti_{0.12}CoSb_{0.8}Sn_{0.2}$, which reduces the price to ~$106/kg, a much more affordable cost.

In order to compare the performance of TE materials, output power generation and its maximum conversion efficiency (η_{max}) is typically calculated by,

$$\eta_{\max} = \frac{T_H - T_C}{T_H} \cdot \frac{\sqrt{1+Z\bar{T}}-1}{\sqrt{1+Z\bar{T}}+\frac{T_C}{T_H}} \quad (1)$$

where T_H, T_C, and $\bar{T}$ is hot side, cold side, and the average temperature, respectively. This is derived from temperature independent TE properties, *i.e.*, constant values through its working temperature. However, this gives a reasonable agreement only when temperature difference is moderate, and the nonlinearity of TE properties with the temperature could generate large error. The peak working temperature of HH is around 700 °C, which might generate temperature gradient as large as 600 °C/2 mm (or higher). Thus, Eq. (1) cannot predict its performance precisely. In this work, numerical analysis[22,23] is carried out to obtain the power generation and efficiency according to temperature dependency of TE properties, where Thomson effect is also taken into account.

2. Experimental details

In this work, we kept the previously optimized amount of Co, Sb and Sn,[1] and focused on tuning the amount of Hf, Zr, and Ti with Hf concentration not exceeding 0.25. Also, the previously reported composition, $Hf_{0.44}Zr_{0.44}Ti_{0.12}CoSb_{0.8}Sn_{0.2}$ was set as a reference. The ingots were formed under Ar protection by arc melting the weighed pure elements (Alfa Aesar, ≥ 99.9% purity) according to the stoichiometry. To guarantee the composition homogeneity, the ingots were melted 3-4 times and flipped over each time. The ingots were then milled to nanopowders by a high energy ball mill (SPEX 8000M Mixer/Mill) in Ar environment for 5 hours. The powders were compacted to disks by a direct current (DC) hot press at 1100-1125 °C and 80 MPa for 2 min. X-ray diffraction (XRD) were employed to determine the phases, both scanning electron microscope (SEM) (LEO 1525) and transmission electron microscope (TEM) (JEOL 2100F) were used to check the grain sizes and microstructures. The thermal conductivity was calculated as a product of the thermal diffusivity (D), bulk density, and specific heat (C_p), which were measured by a laser flash system (LFA 457 Nanoflash, Netzsch Instruments, Inc.), an Archimedes' kit, and a high-temperature differential scanning calorimetry (DSC) instrument (404 C, Netzsch Instruments, Inc.), respectively. The disks were then cut into bars with dimensions about 2 mm × 2 mm × 12 mm, which were measured by a ZEM-3 machine (ULVAC) to get the electrical resistivity (ρ) and Seebeck coefficient (S). The uncertainties of the parameters are 3% on ρ, D, and C_p, and 5% on S; hence the overall uncertainty of ZT is about 11%. Error bars are not used in the plots to increase the readability. The best composition was repeated for at least three times, and the resulting ZT variations are within 5% from run to run.

3. Results and discussion

3.1 $Hf_xZr_{1-x}CoSb_{0.8}Sn_{0.2}$

To determine the favorable amount of Zr usage, initially, the series of $Hf_xZr_{1-x}CoSb_{0.8}Sn_{0.2}$ were synthesized with x varies from 0.15 to 0.25. XRD results indicate the formation of pure HH phase of all the prepared samples (Fig. 1a). SEM and TEM shows the grain sizes vary from 50 to 250 nm (Fig. 1b and 1c). The density measurement (Table

2) indicates that the samples are densely compacted without any porosity. The relative densities that are higher than 100% are from experimental error. All the thermoelectric properties are shown in Fig. 2.

Table 2. Nominal composition, theoretical density, measured density, and relative density

Sample	Nominal Composition	Theoretical Density (g/cm^3)	Measured Density (g/cm^3)	Relative Density
1	$Hf_{0.15}Zr_{0.85}CoSb_{0.8}Sn_{0.2}$	8.383	8.402	100.23%
2	$Hf_{0.2}Zr_{0.8}CoSb_{0.8}Sn_{0.2}$	8.535	8.574	100.46%
3	$Hf_{0.19}Zr_{0.76}Ti_{0.05}CoSb_{0.8}Sn_{0.2}$	8.467	8.45	99.79%
4	$Hf_{0.25}Zr_{0.75}CoSb_{0.8}Sn_{0.2}$	8.648	8.691	100.50%
5	$Hf_{0.44}Zr_{0.44}Ti_{0.12}CoSb_{0.8}Sn_{0.2}$	9.112	9.092	99.78%

We found that all the three compositions (x = 0.15, 0.2, and 0.25) have very similar electrical resistivity and Seebeck coefficient in the whole temperature range (Fig. 2a and 2b). The result is reasonable since the heavily doped element Sn, at the Sb site, has fixed concentration in all the compositions, leading to almost identical nominal carrier concentrations, hence neither the resistivity nor the Seebeck coefficient of each composition would be expected to vary significantly from each other. As a result, similar power factors are observed for the three compositions (Fig. 2c).

Based on the thermal diffusivity (Fig. 2d) and specific heat (Fig. 2e), we found a lowest thermal conductivity with x = 0.25 among all the three compositions, which is the result of relatively stronger alloying effect by increased mass disorder. However, the attenuation of the alloying effect with increasing x was also observed since the thermal conductivity difference between x = 0.2 and x = 0.25 is much smaller than that between x = 0.15 and x = 0.2 (Fig. 2f). We also estimated the lattice thermal conductivity using the Wiedemann–Franz relation, $\kappa_e = \frac{LT}{\rho}$, where κ_e and L are the electronic thermal conductivity and Lorenz constant, respectively. The temperature independent Lorenz numbers are calculated from the reduced Fermi energy derived from the extrapolated Seebeck coefficient at room temperature.[24] The saturation of alloying effect is observed with x increase from 0.2 to 0.25, which is consistent with the calculated result by Shiomi

et al.[25] using Green-Kubo method. Finally, we found similar peak *ZTs* reaching ~0.85 with x = 0.2 and 0.25 at 700 °C (Fig. 2h). Considering our aim to decrease the usage of Hf, the composition with x = 0.2 is more favorable than the one with x = 0.25.

3.2 $Hf_{0.19}Zr_{0.76}Ti_{0.05}CoSb_{0.8}Sn_{0.2}$

Based on the results on $Hf_{0.2}Zr_{0.8}CoSb_{0.8}Sn_{0.2}$ and $Hf_{0.8}Ti_{0.2}CoSb_{0.8}Sn_{0.2}$, where the best *ZT* appears to be with Hf/Zr ratio of 1/4 and Hf/Ti of 4/1, respectively, we specifically come up with the following composition, within which the Hf/Zr ratio is 1/4, and the Hf/Ti ratio is 4/1. Hence we get $Hf_{0.19}Zr_{0.76}Ti_{0.05}CoSb_{0.8}Sn_{0.2}$. The corresponding results, along with the results of $Hf_{0.2}Zr_{0.8}CoSb_{0.8}Sn_{0.2}$ and $Hf_{0.44}Zr_{0.44}Ti_{0.12}CoSb_{0.8}Sn_{0.2}$,[1] are shown in Fig. 3.

Fig. 3a indicates that electrical resistivity of the three compositions are quite different: the one with x = 0.19 has the lowest electrical resistivity and the one with x = 0.44 has the highest value (Fig. 3a), while the Seebeck coefficient of them is similar (Fig. 3b). As a result, the power factor of $Hf_{0.19}Zr_{0.76}Ti_{0.05}CoSb_{0.8}Sn_{0.2}$ is improved a lot comparing with the others in the whole temperature range (Fig. 3c).

On the other hand, based on the diffusivity (Fig. 3d) and specific heat (Fig. 3e), the thermal conductivity of $Hf_{0.19}Zr_{0.76}Ti_{0.05}CoSb_{0.8}Sn_{0.2}$ is similar to that of $Hf_{0.2}Zr_{0.8}CoSb_{0.8}Sn_{0.2}$ (Fig. 3f). Also, from Fig. 3g, we found that the lattice thermal conductivity keeps decreasing with higher concentration of Ti due to the stronger alloying effect. Although $Hf_{0.44}Zr_{0.44}Ti_{0.12}CoSb_{0.8}Sn_{0.2}$ possesses much lower thermal conductivity, as a result of heavier average atomic mass, its *ZT* does not show any advantages comparing with $Hf_{0.19}Zr_{0.76}Ti_{0.05}CoSb_{0.8}Sn_{0.2}$ within the whole temperature range (Fig. 3h), since the lower thermal conductivity (Fig. 3f) of the former is offset by the lower power factor (Fig. 3c). For $Hf_{0.19}Zr_{0.76}Ti_{0.05}CoSb_{0.8}Sn_{0.2}$, the peak *ZT* is about 1.0 at 700 °C, which is basically the same as that of $Hf_{0.44}Zr_{0.44}Ti_{0.12}CoSb_{0.8}Sn_{0.2}$.

To summarize the *ZT*s of the different compositions, we plotted the temperature dependent ZTs of all the compositions we studied in this work and the two references

reported previously in Fig. 4. It is clear that the *ZT*s of new composition $Hf_{0.19}Zr_{0.76}Ti_{0.05}CoSb_{0.8}Sn_{0.2}$ is just as good as that of the previously reported best p-type composition $Hf_{0.44}Zr_{0.44}Ti_{0.12}CoSb_{0.8}Sn_{0.2}$, but the concentration of Hf is much lower, which reduces the price significantly.

Due to the higher power factor, we expect a higher output power from $Hf_{0.19}Zr_{0.76}Ti_{0.05}CoSb_{0.8}Sn_{0.2}$ than $Hf_{0.44}Zr_{0.44}Ti_{0.12}CoSb_{0.8}Sn_{0.2}$ even though the conversion efficiency is similar. A general form of energy balance of a TE leg at one-dimensional heat flow is,

$$\frac{d}{dx}\left(\kappa(x)\frac{dT(x)}{dx}\right)+J^2\rho(x)-JT(x)\frac{dS(x)}{dx}=0 \qquad (2)$$

where the left hand side of Eq. (2) represents heat conduction, Joule heat, and Thomson heat, respectively, and no heat loss is considered. J is current density. In order to solve the differential equation by accounting the temperature dependence of TE properties, a finite difference method is used. A TE leg is divided into n nodes, and a central difference scheme is applied to approximate a temperature and TE properties at each node. This yields a linear relation between nodes as shown in Eq. (3).

$$\frac{\kappa_{i+1}-\kappa_{i-1}}{2\delta x}\cdot\frac{T_{i+1}-T_{i-1}}{2\delta x}+\kappa_i\frac{T_{i+1}-2T_i+T_{i-1}}{\delta x^2}+J^2\rho_i-JT_i\frac{S_{i+1}-S_{i-1}}{2\delta x}=0 \qquad (3)$$

where, $i = 2, 3, \ldots, n\text{-}1$ since T_1 and T_n are known as T_H and T_C, respectively. By iterating until solutions are converged, the numerical analysis is finalized in which the convergence condition of the temperature and electric current in this calculation is 10^{-10}.

Figs. 5a and 5b show a validation of numerical analysis and an effect based on TE properties as a function of temperature where T_H varies from 75 °C to 700 °C while T_C is kept at 50 °C. The analytically simplified calculation has an agreement with the numerical solutions within 2% when ΔT is smaller than 175 °C, but it is overestimated by more than 6% at ΔT = 650 °C. The output power generation of $Hf_{0.19}Zr_{0.76}Ti_{0.05}CoSb_{0.8}Sn_{0.2}$ is improved by 16.7% at ΔT = 650 °C and a = 2 mm as compared with $Hf_{0.44}Zr_{0.44}Ti_{0.12}CoSb_{0.8}Sn_{0.2}$, and it is linearly proportional to the cross-

section area of TE leg (Fig. 5a) while the conversion efficiency has less than 1% difference from each other through the whole temperature range (Fig. 5b), where the maximum efficiency of each material is not a function of the leg dimension *a*.

The ratio of output power to input heat is plotted in Fig. 5c according to various TE leg lengths. Shorter TE leg requires more heat flux to generate a certain temperature difference, and gives rise to larger amount of output power due to its lower electrical resistance of TE leg. In all cases, $Hf_{0.19}Zr_{0.76}Ti_{0.05}CoSb_{0.8}Sn_{0.2}$ requires more heat across TE leg and generates larger electrical power as compared with $Hf_{0.44}Zr_{0.44}Ti_{0.12}CoSb_{0.8}Sn_{0.2}$ because the thermal and electrical conductivities of $Hf_{0.19}Zr_{0.76}Ti_{0.05}CoSb_{0.8}Sn_{0.2}$ are larger through all temperature range.

Fig. 5d shows the effect of the Hf reduction on the output power density and power cost. The use of less Hf element reduces mass density of the alloy as well as the material cost. The hollow marker represents the specific power density, W g^{-1}, and the solid symbols are for the power cost, W $\$^{-1}$. As mentioned, output power of $Hf_{0.19}Zr_{0.76}Ti_{0.05}CoSb_{0.8}Sn_{0.2}$ is improved due to the higher power factor. In addition, The specific power density of $Hf_{0.19}Zr_{0.76}Ti_{0.05}CoSb_{0.8}Sn_{0.2}$ is increased by ~25% along with ~7% reduced mass density, and ~40% reduction of total cost of $Hf_{0.19}Zr_{0.76}Ti_{0.05}CoSb_{0.8}Sn_{0.2}$, which results in an ~91% increase of the electric power generation per dollar by $Hf_{0.19}Zr_{0.76}Ti_{0.05}CoSb_{0.8}Sn_{0.2}$. Therefore, the new composition $Hf_{0.19}Zr_{0.76}Ti_{0.05}CoSb_{0.8}Sn_{0.2}$ is much more favorable for practical applications due to the higher power factor even though the conversion efficiency is the same.

4. Conclusion

Aiming at decreasing the amount of Hf usage, we found the best *ZT* is ~0.85 at 700 °C in $Hf_{0.2}Zr_{0.8}CoSb_{0.8}Sn_{0.2}$. By further replacing some Hf and Zr with Ti, we established a new composition of $Hf_{0.19}Zr_{0.76}Ti_{0.05}CoSb_{0.8}Sn_{0.2}$ to reach a *ZT* of ~1.0 at 700 °C with the Hf/Ti ratio at 4/1 and Hf/Zr ratio at 1/4. These findings enable us to significantly decrease the price of the materials and increase the output power without losing any TE conversion efficiency comparing with the best reported p-type composition, which will greatly

accelerate our commercialization of half-Heusler materials for large scale applications in waste heat recovery.

Acknowledgement

This work is supported by the U.S. Department of Energy under award number DE-EE0004840**.**

References

1 X. Yan, W. S. Liu, S. Chen, H. Wang, Q. Zhang, G. Chen and Z. F. Ren, *Adv. Energy Mater.*, 2013, **3**, 1195–1200.

2 S. Chen, K. C. Lukas, W.S. Liu, C. P. Opeil, G. Chen and Z. F. Ren, *Adv. Energy Mater.,* 2013, **3**, 1210-1214.

3 Y. Z. Pei, X. Y. Shi, A. LaLonde, H. Wang, L. D. Chen and G. J. Snyder, *Nature*, 2011, **473**, 66-69.

4 K. Biswas, J. Q. He, I. D. Blum, C. I. Wu, T. P. Hogan, D. N. Seidman, V. P. Dravid and M. G. Kanatzidis, *Nature*, 2012, **489**, 414-418.

5 Q. Zhang, F. Cao, W. S. Liu, K. Lukas, B. Yu, S. Chen, C. Opeil, D. Broido, G. Chen and Z. F. Ren, *J. Am. Chem. Soc.*, 2012, **134**, 10031-10038.

6 B. Poudel, Q. Hao, Y. Ma, Y. C. Lan, A. Minnich, B. Yu, X. Yan, D. Z. Wang, A. Muto, D. Vashaee, X. Y. Chen, J. M. Liu, M. S. Dresselhaus, G. Chen and Z.F. Ren, *Science*, 2008, **320**, 634-638.

7 X. Shi, J. Yang, J. R. Salvador, M. Chi, J. Y. Cho, H. Wang, S. Bai, J. Yang, W. Zhang and L. Chen, *J. Am. Chem. Soc.*, 2011, **133**, 7837-7846.

8 G. Rogl, D. Setman, E. Schafler, J. Horky, M. Kerber, M. Zehetbauer, M. Falmbigl, P. Rogl, E. Royanian and E. Bauer, *Acta Mater.*, 2012, **60**, 2146-2157.

9 G. Joshi, H. Lee, Y. C. Lan, X. W. Wang, G. H. Zhu, D. Z. Wang, R. W. Gould, D. C. Cuff, M. Y. Tang, M. S. Dresselhaus, G. Chen and Z. F. Ren, *Nano Lett.*, 2008, **8**, 4670-4674.

10 X. W. Wang, H. Lee, Y. C. Lan, G. H. Zhu, G. Joshi, D. Z. Wang, J. Yang, A. J. Muto, M. Y. Tang, J. Klatsky, S. Song, M. S. Dresselhaus, G. Chen and Z. F. Ren, *Appl. Phys. Lett.*, 2008, **93**, 193121(1-3).

11 W. Liu, X. Tan, K. Yin, H. Liu, X. Tang, J. Shi, Q. Zhang and C. Uher, *Phys. Rev. Lett.*, 2012, **108**, 166601.

12 A. Saramat, G. Svensson, A. E. C. Palmqvist, C. Stiewe, E. Mueller, D. Platzek, S. G. K. Williams, D. M. Rowe, J. D. Bryan and G. D. Stucky, *J. Appl. Phys.*, 2006, **99**, 023708

13 L. L. Wang, L. Miao, Z. Y. Wang, W. Wei, R. Xiong, H. J. Liu, J. Shi and X. F. Tang, *J. Appl. Phys.*, 2009, **105**, 013709.

14 C. Yu, T. J. Zhu, R. Z. Shi, Y. Zhang, X, B, Zhao and, J. He, *Acta Mater.*, 2009, **57**, 2757-2764.

15 H. H. Xie, H. Wang, Y. Z. Pei, C. G. F, X. H. Liu, G. J. Snyder, X. B. Zhao and T. J. Zhu, *Adv. Funct. Mater.* 2013, **23**, 5123-5130.

16 S. Sakurada and N. Shutoh, *Appl. Phys. Lett.*, 2005, **86**, 082105.

17 S. Gahlawat, R. He, S. Chen, L. Wheeler, Z. F. Ren, and K. W. White, *J. Appl. Phys.*, 2014, **116**, 083516

18 S. Chen and Z. F. Ren, *Mater. Today*, 2013, **16**, 387-395.

19 G. Joshi, X. Yan, H. Z. Wang, W. S, Liu, G. Chen and Z. F. Ren, *Adv. Energy Mater.*, 2011, **1**, 643–647.

20 USGS, Scientific Investigations Report 2012–5188.

21 X. Yan, W. S. Liu, H. Wang, S. Chen, J. Shiomi, K. Esfarjani, H. Z. Wang, D. Z. Wang, G Chen and Z. F. Ren, *Energy Environ. Sci.*, 2012, **5**, 7543–7548.

22 G. D. Mahan, *J. Appl. Phys.*, 1991, **70**, 4551-4554.

23 T. P. Hogan and T. Shih, in *Thermoelectrics Handbook: Macro to Nano*, ed. D. M. Rowe, CRC Press, Boca Raton (FL), 2006, ch. 12.

24 W. S. Liu, Q. Y. Zhang, Y. C. Lan, S. Chen, X. Yan, Q. Zhang, H. Wang, D. Z. Wang, G. Chen and Z. F. Ren, *Adv. Energy Mater.*, 2011, **1**, 577–587.

25 J. Shiomi, K. Esfarjani and G. Chen, *Phys. Rev. B*, 2011, **84**, 104302.

Figure Captions

Figure 1. a) XRD of $Hf_x(ZrTi)_{1-x}CoSb_{0.8}Sn_{0.2}$, indicating the formation of pure HH phase, b) SEM, and c) TEM image of $Hf_{0.19}Zr_{0.76}Ti_{0.05}CoSb_{0.8}Sn_{0.2}$, which indicate the grain size is of ~50-250 nm.

Figure 2. Temperature dependent thermoelectric properties of $Hf_xZr_{1-x}CoSb_{0.8}Sn_{0.2}$ with x = 0.15, 0.2, and 0.25. a) electrical resistivity; b) Seebeck coefficient; c) power factor; d) thermal diffusivity; e) specific heat, f) thermal conductivity, g) lattice thermal conductivity, and h) *ZT*.

Figure 3. Temperature dependent thermoelectric properties of $Hf_{0.44}Zr_{0.44}Ti_{0.12}CoSb_{0.8}Sn_{0.2}$, $Hf_{0.2}Zr_{0.8}CoSb_{0.8}Sn_{0.2}$ and $Hf_{0.19}Zr_{0.76}Ti_{0.05}CoSb_{0.8}Sn_{0.2}$. a) electrical resistivity; b) Seebeck coefficient; c) power factor; d) thermal diffusivity; e) specific heat, f) thermal conductivity, g) lattice thermal conductivity, and h) *ZT*.

Figure 4. Temperature dependent *ZT* of $Hf_{0.44}Zr_{0.44}Ti_{0.12}CoSb_{0.8}Sn_{0.2}$, $Hf_{0.25}Zr_{0.75}CoSb_{0.8}Sn_{0.2}$, $Hf_{0.2}Zr_{0.8}CoSb_{0.8}Sn_{0.2}$, $Hf_{0.19}Zr_{0.76}Ti_{0.05}CoSb_{0.8}Sn_{0.2}$, and $Hf_{0.15}Zr_{0.85}CoSb_{0.8}Sn_{0.2}$.

Figure 5. Calculated output power density and conversion efficiency dependence of T_H (up to 700 °C) with T_C fixed at 50 °C of $Hf_{0.44}Zr_{0.44}Ti_{0.12}CoSb_{0.8}Sn_{0.2}$ and $Hf_{0.19}Zr_{0.76}Ti_{0.05}CoSb_{0.8}Sn_{0.2}$: comparison of temperature dependent output power density (a) and efficiency (b); c) input and output power relation with the leg length; d) temperature dependent specific power density, W g^{-1}, and power generation cost, W $\$^{-1}$.

a)

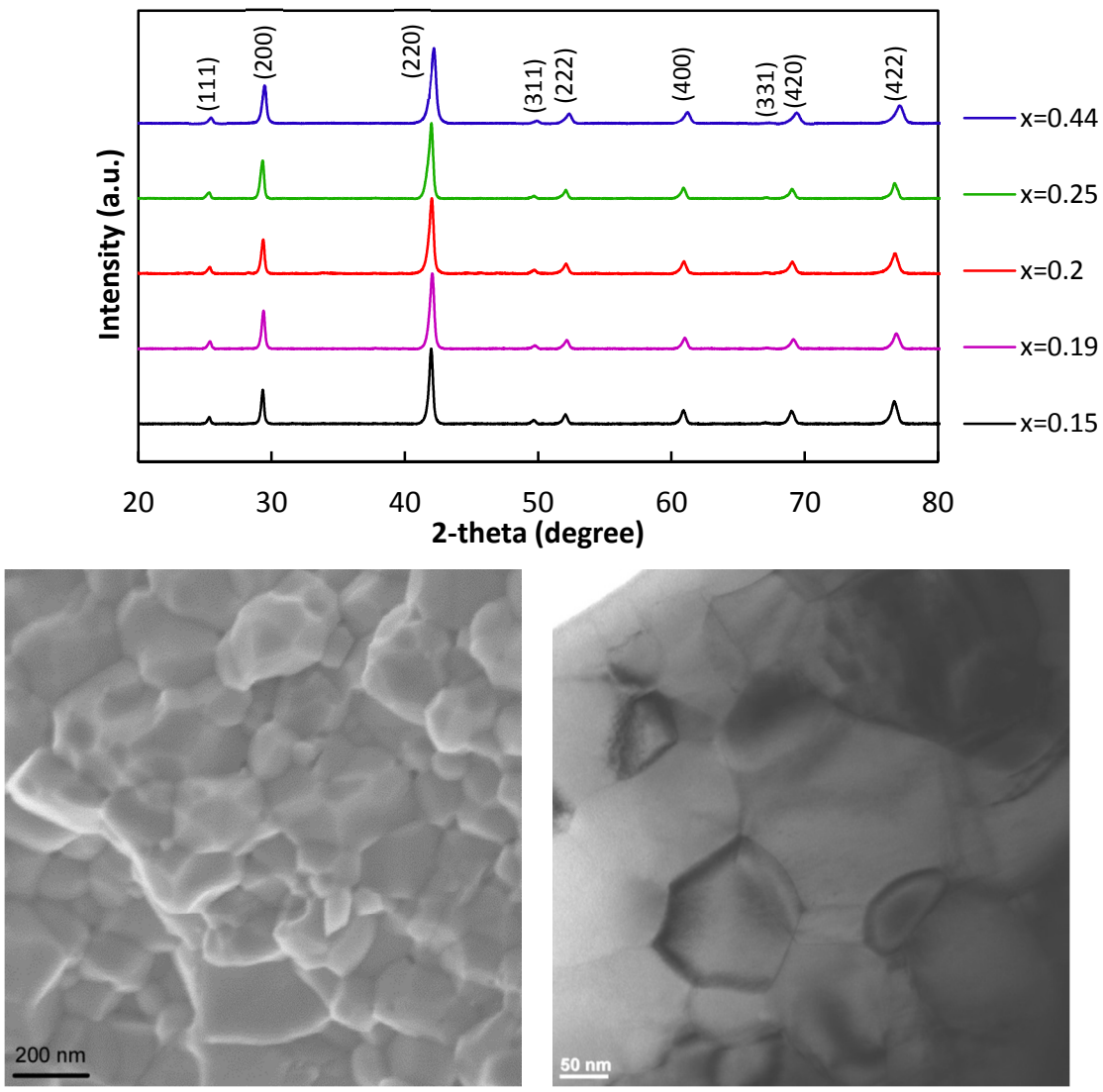

Figure 1. Ran He *et al.*

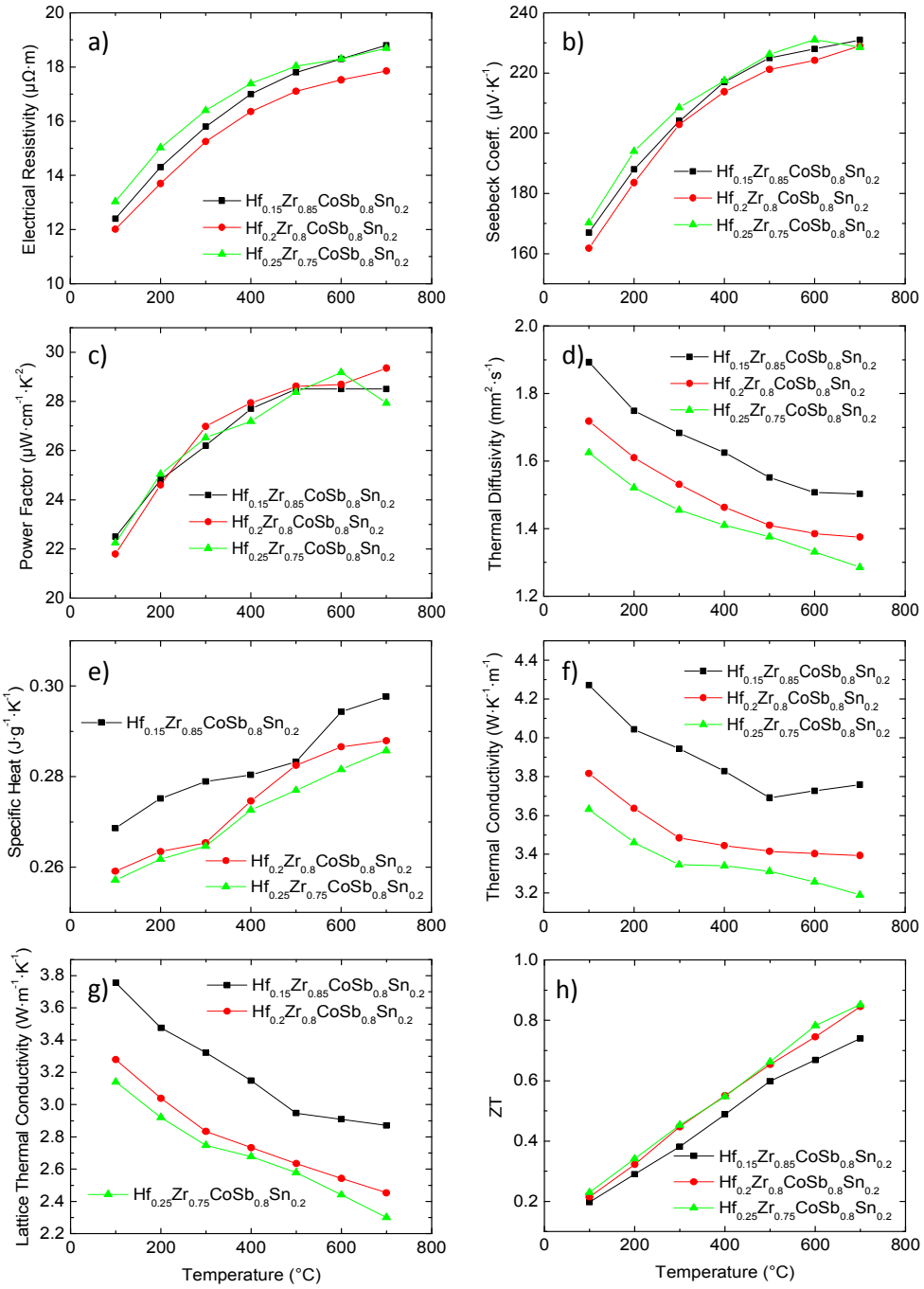

Figure 2. Ran He *et al.*

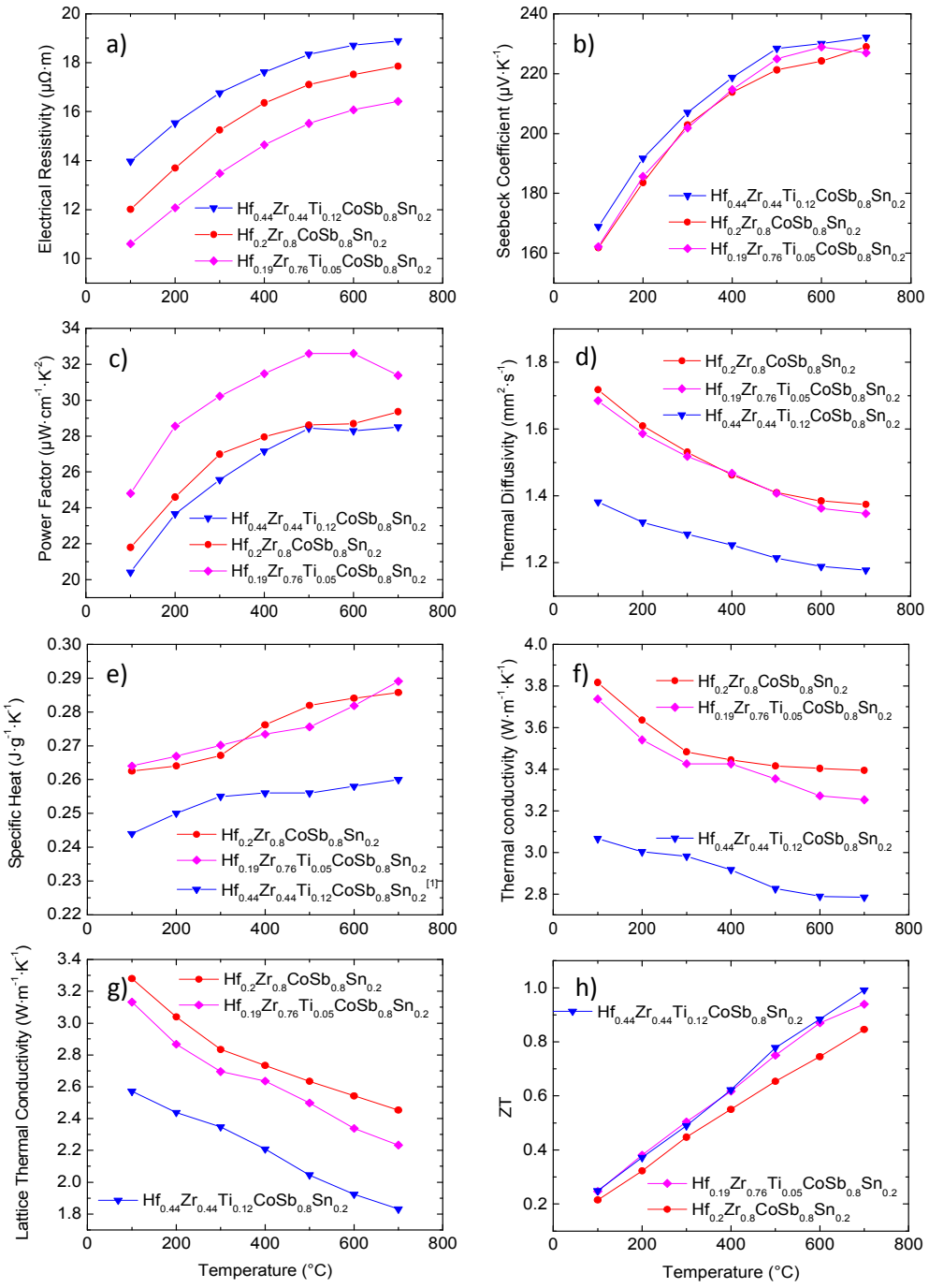

Figure 3. Ran He, *et al*

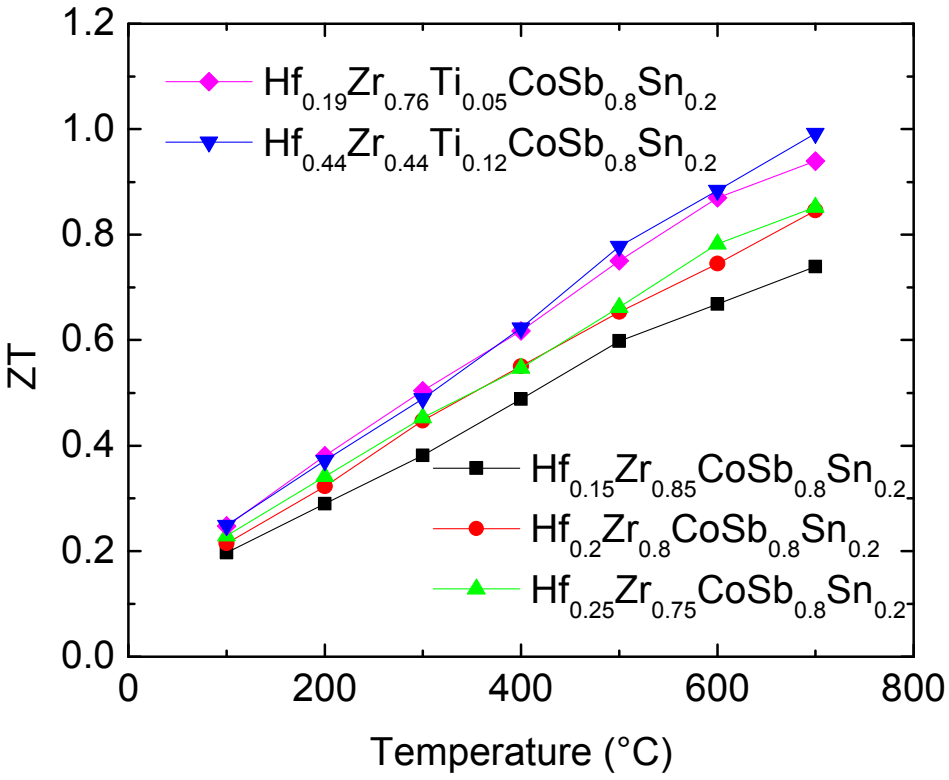

Figure 4. Ran He *et al*.

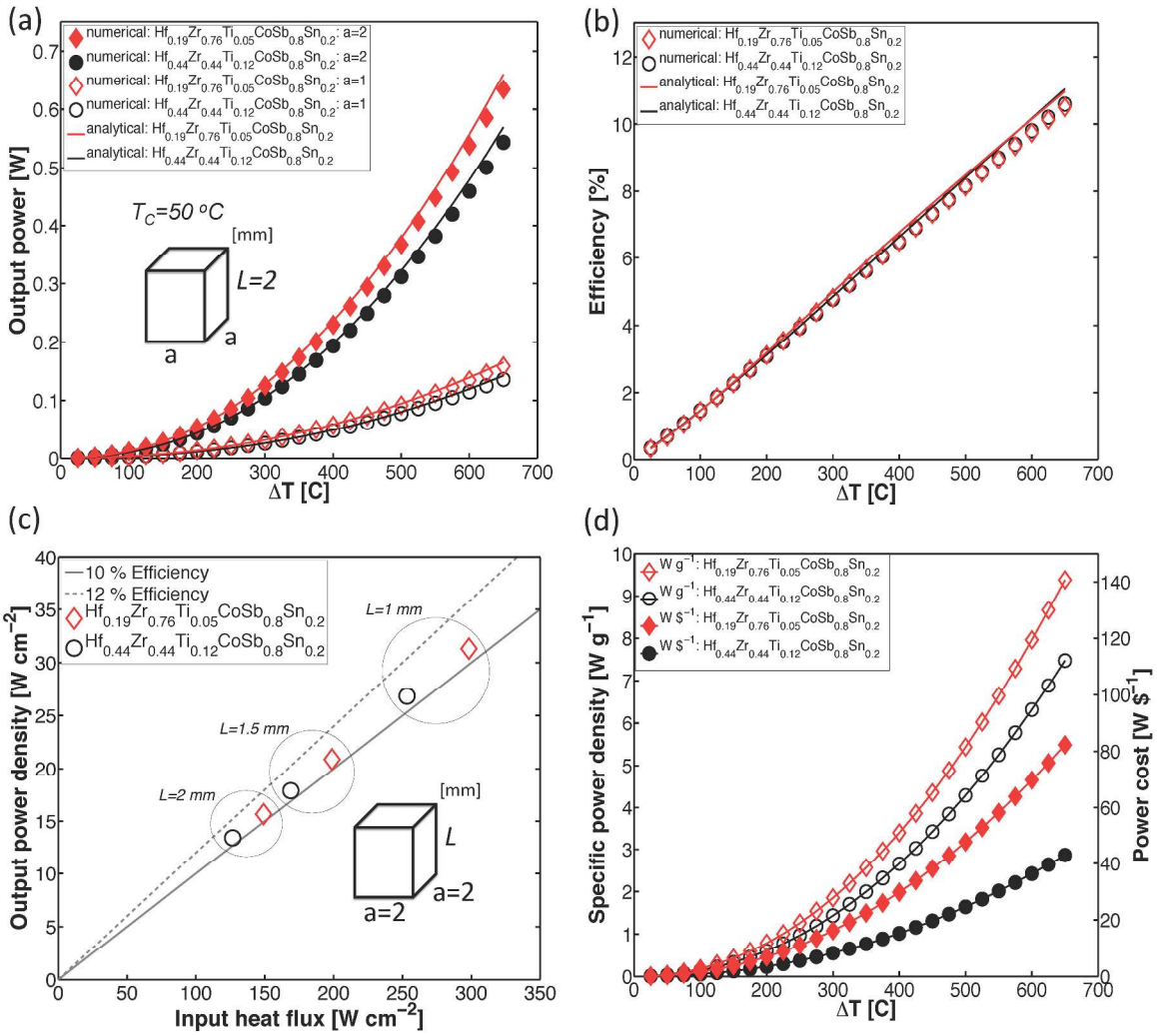

Figure 5. Ran He *et al.*

Figure Captions

Figure 1. a) XRD of $Hf_x(ZrTi)_{1-x}CoSb_{0.8}Sn_{0.2}$, indicating the formation of pure HH phase, b) SEM, and c) TEM image of $Hf_{0.19}Zr_{0.76}Ti_{0.05}CoSb_{0.8}Sn_{0.2}$, which indicate the grain size is of ~50-250 nm.

Figure 2. Temperature dependent thermoelectric properties of $Hf_xZr_{1-x}CoSb_{0.8}Sn_{0.2}$ with x = 0.15, 0.2, and 0.25. a) electrical resistivity; b) Seebeck coefficient; c) power factor; d) thermal diffusivity; e) specific heat, f) thermal conductivity, g) lattice thermal conductivity, and h) *ZT*.

Figure 3. Temperature dependent thermoelectric properties of $Hf_{0.44}Zr_{0.44}Ti_{0.12}CoSb_{0.8}Sn_{0.2}$, $Hf_{0.2}Zr_{0.8}CoSb_{0.8}Sn_{0.2}$ and $Hf_{0.19}Zr_{0.76}Ti_{0.05}CoSb_{0.8}Sn_{0.2}$. a) electrical resistivity; b) Seebeck coefficient; c) power factor; d) thermal diffusivity; e) specific heat, f) thermal conductivity, g) lattice thermal conductivity, and h) *ZT*.

Figure 4. Temperature dependent *ZT* of $Hf_{0.44}Zr_{0.44}Ti_{0.12}CoSb_{0.8}Sn_{0.2}$, $Hf_{0.25}Zr_{0.75}CoSb_{0.8}Sn_{0.2}$, $Hf_{0.2}Zr_{0.8}CoSb_{0.8}Sn_{0.2}$, $Hf_{0.19}Zr_{0.76}Ti_{0.05}CoSb_{0.8}Sn_{0.2}$, and $Hf_{0.15}Zr_{0.85}CoSb_{0.8}Sn_{0.2}$.

Figure 5. Calculated output power density and conversion efficiency dependence of T_H (up to 700 °C) with T_C fixed at 50 °C of $Hf_{0.44}Zr_{0.44}Ti_{0.12}CoSb_{0.8}Sn_{0.2}$ and $Hf_{0.19}Zr_{0.76}Ti_{0.05}CoSb_{0.8}Sn_{0.2}$: comparison of temperature dependent output power density (a) and efficiency (b); c) input and output power relation with the leg length; d) temperature dependent specific power density, W g^{-1}, and power generation cost, W $\$^{-1}$.

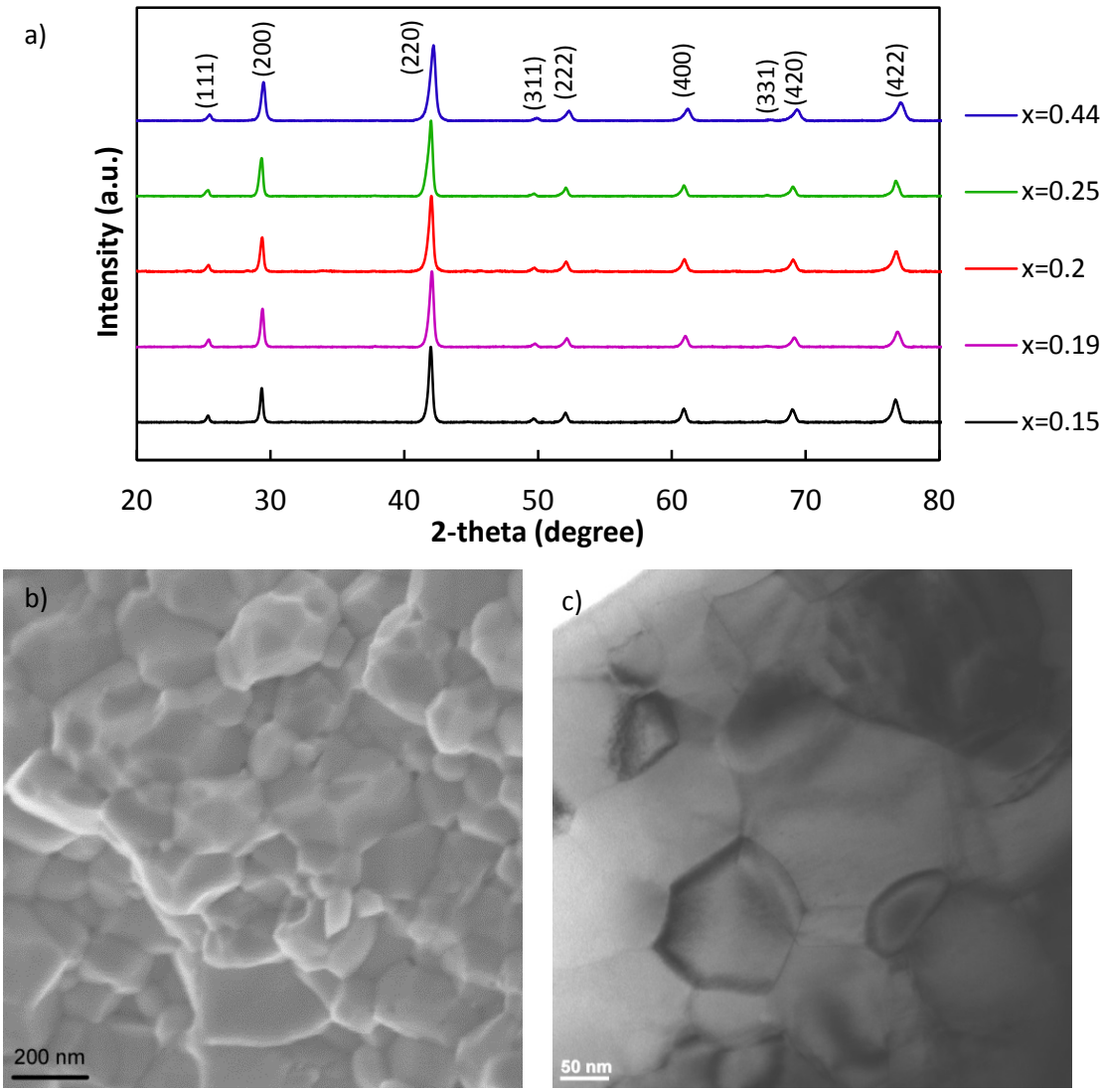

Figure 1. Ran He *et al.*

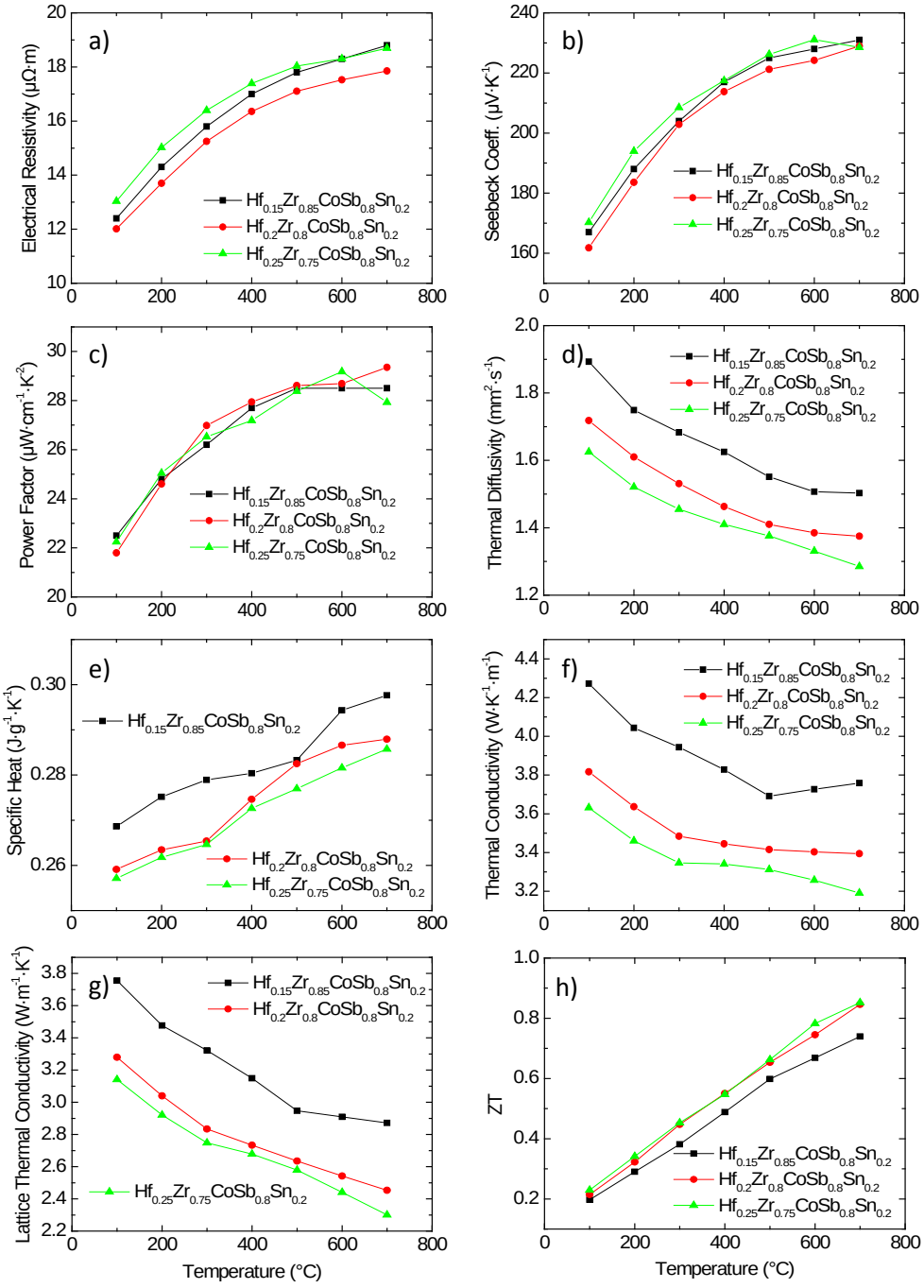

Figure 2. Ran He *et al.*

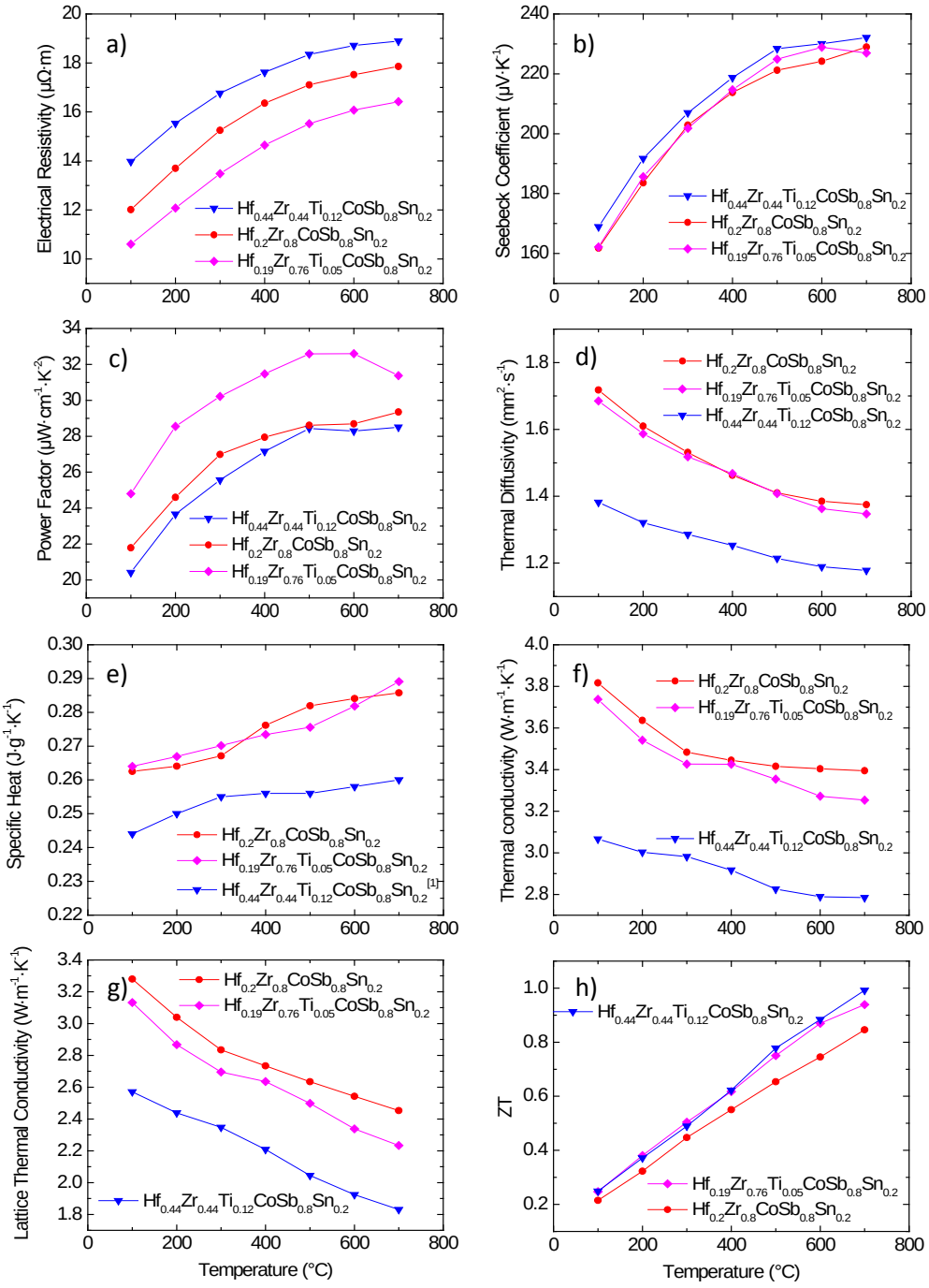

Figure 3. Ran He, *et al*

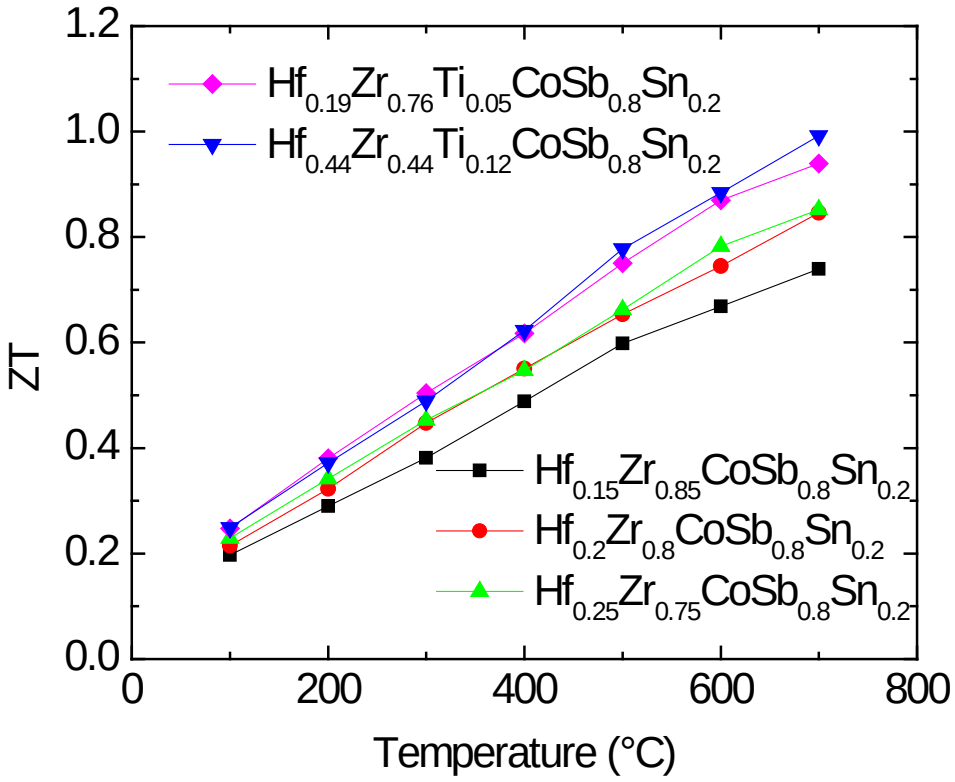

Figure 4. Ran He *et al*.

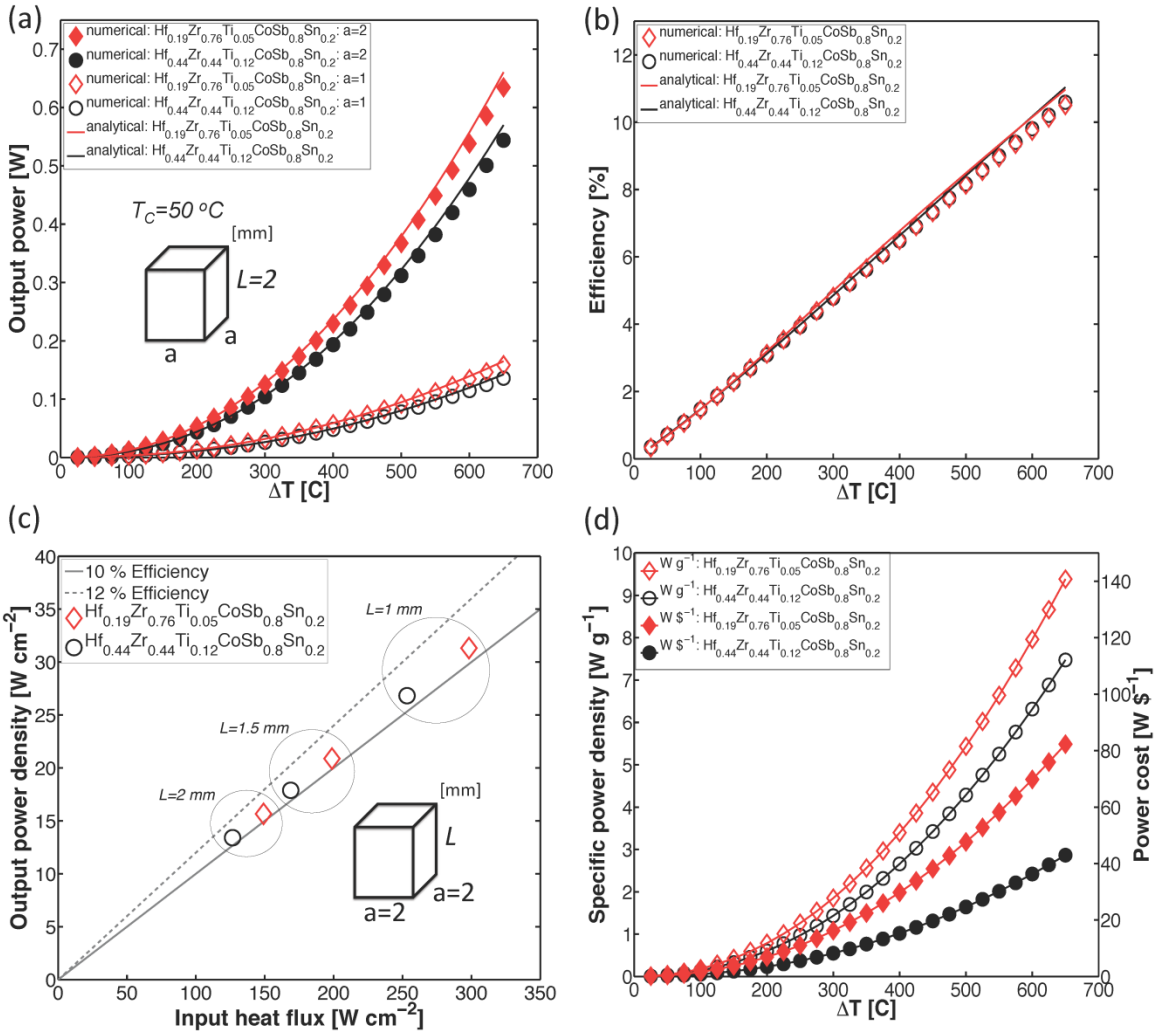

Figure 5. Ran He *et al.*